Christoffer D. Hystad

The title of your master's thesis should be written here

Any undertitle is written here

NTNU

ABSTRACT

Write an abstract/summary of your thesis, and state your main findings here.

A summary should be included in both English and any second language, if this is applicable, regardless if the thesis is written in English or in your preferred language. These should be on separate pages, the English version first.

PREFACE

Write the preface of your thesis here.

You may include acknowledgements and thanks as part of your preface on this page, or you may add it as a new chapter after the preface.

CONTENTS

LIST OF FIGURES

LIST OF TABLES

ONE

INTRODUCTION

1.1   Background & Motivation

Global Navigation Satellite Systems (GNSS) have become deeply embedded into our modern infrastructure with multiple constellations, such as GPS, GLONASS, Galileo and BeiDou, ensuring that four satellites are observable from the surface at any given time, thus providing worldwide coverage [1]. The sheer number of operational satellites that broadcast GNSS signals makes it one of the most powerful signals of opportunity for remote sensing, enabling monitoring without the need for onboard transmitters.
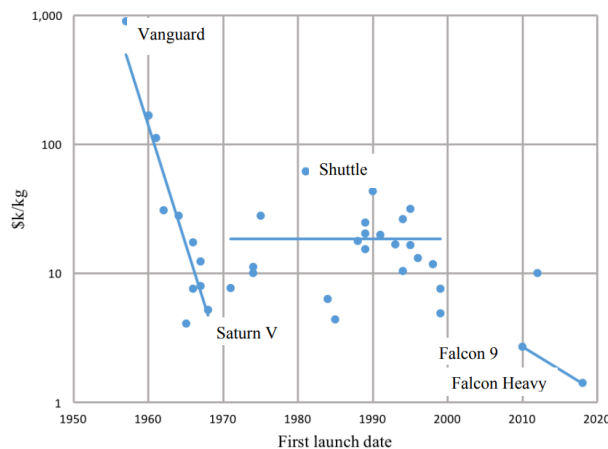
Figure 1.1.1: Launch cost per kilogram to LEO versus first launch date, courtesy of [2]

At the same time, the space sector has recently undergone rapid changes. Launch costs have fallen significantly due to government outsourcing of launch providers to private companies, and the competitive environment it produced. This is clearly shown in figure 1.1.1, where the per-kilogram launch cost has hit an all-time low with the deployment of

SpaceX rockets *Falcon9* and *Falcon Heavy* [2]. As a result, it has become increasingly feasible for universities, research groups and smaller nations to deploy space-based systems dedicated to leveraging GNSS signals for remote sensing applications.

In parallel with this growth, there has also been an increase in the frequency of reported intentional GNSS interference to disrupt aviation operations. The interference can be divided into separate categories characterized by their difference in method and effect: *Jamming* refers to the relative high-power emission of Radio Frequency (RF) noise to block GNSS signals, while *spoofing* is the transmission of signals that resemble those from real satellites, misleading the GNSS receiver to think it has a different position [3]. The Norwegian Defense Research Establishment (FFI) states that: "In Norway's northernmost county of Finnmark, close to the Russian border, loss of GNSS signals due to jamming occurs nearly daily. [...] The number of disruptions has increased significantly since Russia's invasion of Ukraine in 2022." [4]. Data from *gpsjam.org* suggest that similar disruptions have been reported across Eastern Europe, the Middle East, and the Arctic [5]. These events highlight a broader geopolitical trend: GNSS interference is becoming more common. This places increased strategic value on systems that can detect and localize jamming and spoofing events.

GNSS Reflectometry (GNSS-R) offers a promising technique for addressing these challenges. According to Jin and Komjathy [6], Hall and Cordey [7] were the first to propose that GNSS L-band reflections could be exploited in a bistatic radar configuration to retrieve ocean surface properties, laying the foundation for modern GNSS-R techniques. Recent theory suggest that the same bistatic configuration can be used for surveillance of the GNSS spectrum, where multiple GNSS-R satellites in formation can detect and localize sources of jamming and spoofing. This emerging use-case is one of the central research goals of NTNU SmallSat Lab's GNSS-R project, which aim to develop methods for this process [8]. The project currently investigates this concept through its GNSS-R satellite mission study, exploring formations geometries, orbit configurations and system designs that would enable robust detection of GNSS interference sources and ships.

Accurate knowledge of spacecraft position and velocity is essential for the performance of any GNSS-R system. In such systems, regardless of application, the reflected GNSS signal is interpreted by comparing its time delay and Doppler shift relative to the direct signal. This process is highly sensitive to the specular reflection point's geolocation, which is given by the geometric relationship between the GNSS transmitter, the reflecting surface and the receiver. Even small errors in the satellite's propagated state shifts the estimated specular point by kilometers. Such errors can lead to misinterpretations of the delay-Doppler maps, for instance if the predicted specular point is over ocean when the true specular point occurs over land [9].

In real missions, the satellite orbit and relative geometry within satellite formations will naturally drift over time due to orbital perturbations. During mission design, simulation tools are used to predict the satellites motion. If the simulation does not accurately model the relevant perturbations, its predicted state evolution will diverge from physically realistic behavior, eventually yielding incorrect specular point locations and misleading conclusions about the performance of the GNSS-R system. Furthermore, inaccuracies in position and velocity directly translates to uncertainty in later analyses, like coverage analysis, or formation-keeping delta-V estimation. For these reasons, a high-fidelity

propagator is necessary to ensure realistic and reliable evaluations of the GNSS-R system performance.

1.2 Problem Definition

A system simulator has already been developed to support the development of SmallSat Lab's GNSS-R project (cite???). The tool currently allows area coverage estimation and a detection probability analysis of a stationary maritime target, and is intended to be extended for ocean surveillance and GNSS Radio Frequency interference (RFI) detection in the future. As explored in the previous section, these analyses rely on accurately propagating both GNSS and GNSS-R satellites to minimize their uncertainties. Currently, the simulator uses the SGP4 propagator through the Skyfield Python library for this purpose.

The SGP4 propagator has long been the industry standard for orbit prediction, and has subsequently been the subject of thorough evaluation. Several studies document that the propagator can exhibit decreasing accuracy over longer time-horizons, particularly for formation-flight or precision geometry applications [10]. This raises concerns about whether the current SGP4-based implementation is sufficiently accurate for GNSS-R studies, which are highly sensitive to orbital state errors.

1.2.1 Project Formulation

This motivates a systematic verification of the Skyfield-SGP4 implementation by comparing its long-term predictions against a propagator with higher modeling fidelity. Therefore, this specialization project will support the SmallSat Lab GNSS-R mission by developing such a propagator within the Basilisk simulation framework, which natively supports detailed perturbation models and allows for controlled comparisons with Skyfield-SGP4. The study uses this capability to evaluate the differences between the propagators and evaluate their implications for GNSS-R mission analysis. As a result, the project is guided by three research questions:

- What is the intrinsic numerical difference between the Skyfield-SGP4 and the Basilisk frameworks when configured identically?

- How does the introduction of extended perturbation models influence the divergence between the propagators over time?

- How do differences in simulated translational states affect formation-keeping analyses?

Answering these questions will support the project's goal of guaranteeing the reliability and accuracy of orbital propagation tools used for GNSS-R small-satellite formation studies in future mission design.

1.3 Overall Method

1.4 Project Scope & Limitations

This specialization project focuses on evaluating the long-term orbital propagation accuracy of two distinct simulation frameworks, Skyfield-SGP4 and a high-fidelity Basilisk propagator, in the context of GNSS-R formation-flying missions. To ensure a controlled and way defined comparison, the project's scope has been limited to a set of simulation configurations and perturbation models.

1.4.1 Simulation Configuration Scope

The analysis covers a relatively long time-horizon, ranging from several days up to one week, in order to adequately capture the frameworks' divergence over a mission-relevant time span. The simulated formation consists of two satellites flying in Low Earth Orbit (LEO) in a leader-follower configuration. Both are initialized on the same orbital plane with nominally constant along-track separation and with the same initial conditions to guarantee same-case comparisons.

1.4.2 Perturbation Modelling Scope

The Basilisk propagator incorporates a selection of the most influential orbtial perturbation effects in LEO:

- Earth's gravity field represented through J2-J4 spherical harmonics,

- Atmospheric drag using an exponential density model,

- Cannonball Solar Radiation Pressure (SRP) model with a fixed reflectivity coefficient, and

- third-body gravitational pull from the Sun and Moon

1.4.3 Propagation Tool Scope

The Skyfield–SGP4 implementation serves as the baseline, while Basilisk is used as the higher-fidelity reference. Each framework is configured to propagate identical initial conditions, allowing direct numerical comparison of state evolution over the defined time interval.

1.4.4   Limitations

Several aspects of GNSS-R mission analysis lie outside the scope of this specialization project. First, no attitude dynamics are modeled. The satellites are assumed to maintain a fixed nadir-oriented attitude or otherwise idealized pointing, which removes attitude-orbit coupling and optical or RF pointing constraints from consideration.

Second, the project includes no GNSS-R signal modeling or bistatic radar simulation. The study evaluates orbital geometry only; signal processing elements such as delay-Doppler map generation, specular-point reflectivity, link budget modeling, or interference detection algorithms fall beyond the project's objectives.

Third, no active formation-keeping control is implemented. The satellites follow purely ballistic trajectories under the applied perturbations. As such, the delta-V analysis is limited to estimating how often and how strongly formation drift would need to be corrected, rather than simulating actual guidance, navigation, and control (GNC) actions.

Finally, conclusions drawn from this study are limited to the tested scenarios. The orbital regimes, perturbation models, and formation geometry considered here may not generalize to all LEO missions, nor to GNSS-R concepts employing different formation layouts, attitude profiles, or operational constraints.

These limitations naturally define the boundary between the present specialization project and a potential master's thesis. While this project focuses on verifying orbital propagation fidelity, a master's thesis could extend the analysis by incorporating full attitude modeling, GNSS-R signal simulation, operational formation-keeping strategies, and end-to-end detection performance. Such expansions would build upon the validated propagation models developed here, enabling a more comprehensive assessment of GNSS-R formation-flying missions.

1.5   Report Structure

Following is a brief overview of chapters in this report, and what each of them cover.

TWO

LITERATURE REVIEW

Although astrodynamics is rooted in centuries of celestial mechanics, it only recently emerged as a distinct scientific discipline. As outlined by Szebehely's historical account of the field [11], the development of astrodynamics may be divided into four broad periods: the pre-Newtonian era, the classical or Newtonian period, the contributors from the nineteenth century and finally the rapid expansion that took place in the twentieth century. Although its conceptual roots stretch back to ancient astronomers such as Aristotle and Hipparchus, and its mathematical foundations were laid by Newton's *Principia* [12], Szebehely emphasizes that the practical astrodynamics discipline concerned with applying celestial and ballistic mechanics to artificial bodies, was only formed in the early 1930s. Following the second world war, the field saw rapid growth due to Soviet launch of the *Sputnik* satellite in 1957, and the ensuing space race. With the introduction of more powerful digital computers in the 1960s, Brouwer, Herrick and others led research teams that laid the foundation for analytical and numerical orbit propagation.

Building on this historical foundation, the field has continued to evolve through substantial research effort aimed at increasing predictive accuracy. This trend is indicated by the sharp increase in published work since the early 1990s proposing improved numerical integration methods, orbital propagation schemes and disturbance models. This chapter therefore provides an overview of the theoretical foundations and prior research relevant to this project that have been published after 1960. To provide structure while keeping the scope focused, the review is divided into four themes, each covering aspects of astrodynamics whose understanding is essential for addressing the research questions presented in Section ??. The first theme covers analytical and numerical orbital propagation methods and studies assessing their intrinsic accuracy. The second theme examines orbital perturbation models, specifically gravity-field perturbations, atmospheric drag and SRP. These two themes together provide the methodological background for understanding the differences between the Skyfield SGP4 baseline and the relatively high-fidelity Basilisk implementations.

The third theme envelops the error growth and propagation stability of propagators with a

focus on long-term orbit prediction accuracy, sensitivity to perturbation-model fidelity and numerical integration error. Finally, the forth theme covers satellite formation-keeping, and reviewing how absolute propagation error translate into inaccuracies in relative-state predictions and, consequently, into differences in delta-V estimates for formation maintenance. The last two themes is directly related to the project's investigation of how simulator differences evolve over time, and will provide the theory necessary to understand discrepancies between propagations.

The purpose of this literature review is to map the existing knowledge that supports the analysis carried out in this project. The aim is not to identify research gaps or propose new theoretical developments, but rather provide the theoretical background needed to understand the propagation methods, orbital perturbations and mechanisms causing prediction error over longer time-horizons, which are covered in depth in chapter 3. This mapping of established models and methods also serves to contextualize their relative accuracies, forming the foundation for the simulation-based comparison presented in later chapters.

2.1 Orbital Propagation

2.1.1 Analytical Propagation (SGP4)

Analytical orbit propagation methods rely on closed-form or series-based approximations of the perturbing forces acting on an artificial satellite. Among these, the SGP4 algorithm is the most widely used and has become the de facto standard for propagating publicly distributed Two-Line Element (TLE) sets. As described in detail by Vallado [13], SGP4 operates on mean orbital elements rather than osculating elements, and applies a sequence of analytical corrections to account for dominant perturbations. These corrections include secular and periodic contributions from the Earth's oblateness, simplified treatments of atmospheric drag, and, in some cases, resonance effects. Because the dynamics are expressed through closed-form perturbation series, SGP4 achieves exceptional computational speed and remains efficient even when used to propagate thousands of objects, which has contributed significantly to its long-standing operational use.

Despite these advantages, the analytical nature of SGP4 introduces several well-known limitations. Since the algorithm uses simplified perturbation models and a low-fidelity representation of atmospheric drag, its accuracy deteriorates over longer time horizons, especially in low Earth orbit where drag and solar radiation pressure can drive significant deviations from the mean-element trajectory. Liu *et al.* [14] demonstrate this behaviour empirically, showing that the difference between SGP4 predictions and high-fidelity numerical ephemerides grows noticeably with propagation time. Their work further illustrates how machine-learning techniques can be used to correct these long-term deviations, highlighting the underlying structural limitations of the analytical model. Similarly, Conkey and Zielinski [15] compare classical SGP4 with the extended-precision SGP4-XP variant, showing that improved analytical treatments of atmospheric drag, resonance terms and solar radiation pressure can offer measurable accuracy gains, particularly outside low Earth orbit.

More broadly, studies comparing with high-precision numerical propagators provide valuable insight into the intrinsic accuracy of analytical propagation. Acciarini *et al.* [16] analyse the divergence between SGP4 and a high-fidelity numerical integrator that models detailed perturbations, demonstrating that the differences become increasingly significant over multi-day time spans. Their findings reinforce a key conclusion from the broader literature: while SGP4 is sufficiently accurate for short-term prediction and catalog maintenance, its underlying modelling assumptions impose fundamental limits on long-term orbit fidelity.

In this project, the `Skyfield` Python library is used to provide a baseline trajectory representation, and its implementation relies directly on SGP4 for propagating TLE-based initial conditions. As a result, the SGP4 model serves as the analytical benchmark against which the extended high-fidelity `Basilisk` simulations are compared in later chapters.

2.1.2   Numerical Orbit Propagation

2.1.3   Semianalytical and Hybrid Propagators

2.1.4   Propagator Comparison and Validation

2.2   Orbital Perturbation Modelling

2.2.1   Gravity-Field Perturbations

2.2.2   Atmospheric Drag

2.2.3   Solar Radiation Pressure

2.2.4   Third-Body Perturbations

2.3   Error Growth and Propagation Stability

2.3.1   Long-Term Orbit Prediction Accuracy

2.3.2   Sensitivity to Force-Model Fidelity

2.3.3   Numerical Integration Error

2.3.4   Regime-Dependent Error Growth

2.4   Satellite Formation Flying and Relative Motion

2.4.1   Relative Motion Dynamics

2.4.2   Sensitivity of Relative Motion to Propagation Error

2.4.3   Formation-Keeping delta-V Requirements

2.4.4   Disturbance Effects on Formation Stability

2.5   Summary of Literature Review

Table 2.5.1: Literature overview for the *Orbital propagation* theme

Field	Literature
Analytical propagation (SGP4)	Vallado (2021) Liu *et al.* (2021) Conkey & Zielinski (2022) Acciarini *et al.* (2024)
Numerical orbit propagation	Brouwer & Clemence (1961) Bate, Mueller & White (1971) Battin (1999) Montenbruck & Gill (2000) Vallado (2025)
Semianalytical / hybrid propagators	Kaula (1966) Conkey & Zielinski (2022) Wang *et al.* (2024)
Propagator comparison & validation	Roscoe *et al.* (2014) Liu *et al.* (2021) Conkey & Zielinski (2022) Acciarini *et al.* (2024) Vallado (2025)

Table 2.5.2: Literature overview for the *Orbital perturbation modelling* theme

Field	Literature
Gravity-field perturbations	Kaula (1966) Battin (1999) Montenbruck & Gill (2000) Wakker (2015) Vallado (2021) Wang *et al.* (2024)
Atmospheric drag	Montenbruck & Gill (2000) Roscoe *et al.* (2014) Vallado (2021)
Solar radiation pressure (SRP)	Wertz (1978) Montenbruck & Gill (2000) Roscoe *et al.* (2014) Vallado (2021)
Third-body perturbation	Wertz (1978) Montenbruck & Gill (2000) Roscoe *et al.* (2014) Vallado (2021)

Table 2.5.3: Literature overview for the *Error growth & propagation stability* theme

Field	Literature
Long-term orbit prediction accuracy	Liu *et al.* (2021) Conkey & Zielinski (2022) Acciarini *et al.* (2024) Vallado (2025)
Sensitivity to force-model fidelity	Roscoe *et al.* (2014) Vallado (2021) Conkey & Zielinski (2022) Acciarini *et al.* (2024) Wang *et al.* (2024)
Numerical integration error	Bate, Mueller & White (1971) Battin (1999) Montenbruck & Gill (2000) Vallado (2021)
Regime-dependent error growth	Roscoe *et al.* (2014) Conkey & Zielinski (2022) Vallado (2025)

Table 2.5.4: Literature overview for the *Satellite formation flying* theme

Field	Literature
Relative motion dynamics	Montenbruck & Gill (2000) Schaub & Junkins (2003) Kristiansen *et al.* (2007)
Sensitivity of relative motion to propagation error	Kristiansen *et al.* (2007) Roscoe *et al.* (2014) Vallado (2021)
Formation-keeping ΔV requirements	Kristiansen *et al.* (2007) Roscoe *et al.* (2014)
Disturbance effects on formation stability	Kristiansen *et al.* (2007) Roscoe *et al.* (2014)

THEORY

3.1 Reference Frames

A reference frame is uniquely described by $\mathcal{F}^{rf} : \{\mathcal{O}_{rf}; \hat{\mathbf{x}}_{rf}, \hat{\mathbf{y}}_{rf}, \hat{\mathbf{z}}_{rf}\}$ where $\mathcal{O}_{rf}$ is the origin, and $\{\hat{\mathbf{x}}_{rf}, \hat{\mathbf{y}}_{rf}, \hat{\mathbf{z}}_{rf}\}$ denote the dextral orthogonal unit vectors [17]. In this work, mainly two reference frames are used: the Earth-Centered Inertial (ECI) frame and the Radial-Transverse-Normal (RTN) frame, which is illustrated by Figure 3.1.1. The ECI frame is the inertial frame used to express all absolute satellite motion about the Earth, while the RTN frame provides a satellite-centered frame of reference suited for expressing relative motion within a formation. Lastly, because gravitational and geophysical models are naturally defined in an Earth-fixed coordinate system, a third frame, the Earth-Centered Earth-Fixed (ECEF) frame, is also introduced.
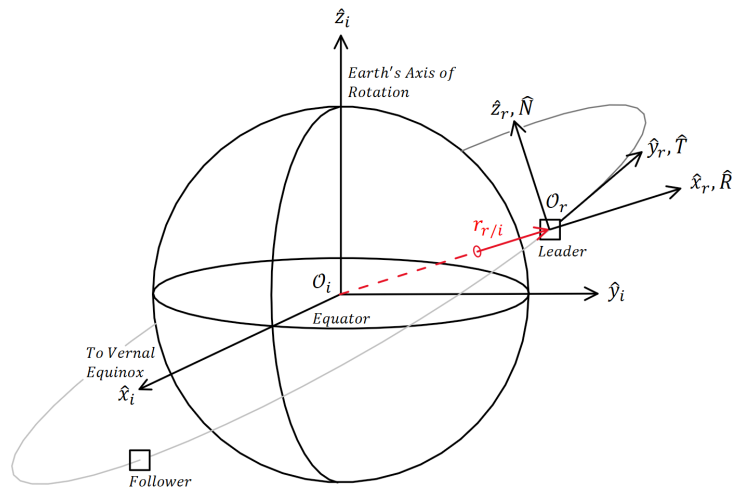

Figure 3.1.1: Illustration of the Earth-Centered Inertial ($\mathcal{F}^i$) and Radial-Transverse-Normal ($\mathcal{F}^r$) frames used in this project. The unit vectors have different length for illustrative purposes. Adapted from [18, 19]

3.1.1 Earth-Centered Inertial (ECI) Frame

The ECI frame, $\mathcal{F}^i : \{\mathcal{O}_i \,; \hat{\mathbf{x}}_i \,, \hat{\mathbf{y}}_i \,, \hat{\mathbf{z}}_i\}$, has its origin at the Earth's Center of Mass (CM) and fixed principal axes relative to the celestial sphere. At any given time, $\hat{\mathbf{x}}_i$ points towards the Vernal Equinox, per definition striking through the equator. $\hat{\mathbf{z}}_i$ points along the Earth's axis of rotation through its geographical North-Pole, and $\hat{\mathbf{y}}_i$ is defined using the right-hand rule. An illustration showing this principal axis configuration is shown in figure 3.1.1. The position of an arbitrary satellite, s, relative to the Earth's CM can then be expressed by its principal components in the ECI frame with the following notation:

$$\mathbf{r}^i_{s/i} = a\hat{\mathbf{x}}^i_i + b\hat{\mathbf{y}}^i_i + c\hat{\mathbf{z}}^i_i = \begin{bmatrix} a & b & c \end{bmatrix}^T \tag{3.1}$$

3.1.2 Radial-Transverse-Normal (RTN) Frame

The RTN frame, $\mathcal{F}^r : \{\mathcal{O}_r \,; \hat{\mathbf{x}}_r \,, \hat{\mathbf{y}}_r \,, \hat{\mathbf{z}}_r\}$, is defined with its origin at the leader's CM in a leader-follower satellite formation. Using l to denote the leader satellite, the frame's orthogonal dextral unit vectors can be defined in the ECI frame as:

$$\hat{\mathbf{R}}^i = \hat{\mathbf{x}}^i_r = \frac{\mathbf{r}^i_{l/i}}{||\mathbf{r}^i_{l/i}||}, \qquad \hat{\mathbf{N}}^i = \hat{\mathbf{z}}^i_r = \frac{\mathbf{r}^i_{l/i} \times \mathbf{v}^i_{l/i}}{||\mathbf{r}^i_{l/i} \times \mathbf{v}^i_{l/i}||}, \qquad \hat{\mathbf{T}}^i = \hat{\mathbf{y}}^i_r = \hat{\mathbf{z}}^i_r \times \hat{\mathbf{x}}^i_r \tag{3.2}$$

Here, $\hat{\mathbf{x}}^i_r$ is the radial unit vector, pointing outwards along the leader's position vector. $\hat{\mathbf{z}}^i_r$ points in the direction orthogonal to $\{\mathbf{r}^i_{l/i}, \mathbf{v}^i_{l/i}\}$ and corresponds to the cross-track direction. Finally, $\hat{\mathbf{y}}^i_r$ is defined through the right-hand rule, giving the along-track direction. An illustration of these definitions is presented in Figure 3.1.1. Using this definition, the transformations to ECI from RTN and back is given by:

$$\mathbf{R}^i_r = \begin{bmatrix} \hat{\mathbf{x}}^i_r & \hat{\mathbf{y}}^i_r & \hat{\mathbf{z}}^i_r \end{bmatrix}, \qquad \mathbf{R}^r_i = (\mathbf{R}^i_r)^T \tag{3.3}$$

3.1.3 Earth-Fixed Earth-Centered (ECEF) Frame

The ECEF frame, $\mathcal{F}^f : \{\mathcal{O}_f \,; \hat{\mathbf{x}}_f \,, \hat{\mathbf{y}}_f \,, \hat{\mathbf{z}}_f\}$, is a rotating Earth-fixed frame with its origin at the Earth's CM. The axis $\hat{\mathbf{z}}^f = \hat{\mathbf{z}}^i$ aligns with the Earth's mean rotation axis, $\hat{\mathbf{x}}^f$ lies on the intersection of the equator and prime meridian, and $\hat{\mathbf{y}}^f$ follows by the right-hand rule. Because the frame rotates with the Earth, the transformation between ECI and ECEF depends on time. This work adopts the formulation of Stryjewski [20], expressing the rotation about the inertial $\hat{\mathbf{z}}^i$-axis through a time-varying angle $\theta(t)$, which is zero at the J2000 epoch (1 January 2000, 12:00 TT). The corresponding rotation matrix is

$$\mathbf{R}^f_i = \begin{bmatrix} \cos\theta(t) & -\sin\theta(t) & 0 \\ \sin\theta(t) & \cos\theta(t) & 0 \\ 0 & 0 & 1 \end{bmatrix}, \qquad \mathbf{R}^i_f = (\mathbf{R}^f_i)^T \tag{3.4}$$

with the rotation angle defined as

$$\theta(t) = \omega \left(GMST(t) - (UT1(t) - UTC(t)) \right), \qquad \omega = 0.261799387799149 \text{ rad/h}. \tag{3.5}$$

3.2   Orbital Perturbations
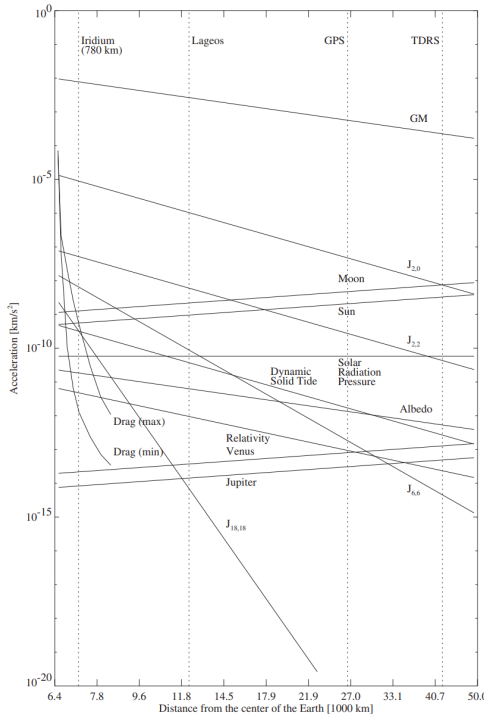
Figure 3.2.1: Order of magnitude of various perturbations of a satellite orbit. Courtesy of [21]

3.2.1   Spherical Harmonics

Assuming the Earth's mass is concentrated in the ECI frame's origin, the acceleration experienced by a spacecraft, s, can be modelled using Newton's gravitational law:

$$\mathbf{a}_{grav} = \left(\ddot{\mathbf{r}}_{s/i}\right)_{grav} = -\frac{\mu}{||\mathbf{r}_{s/i}||_2^3}\mathbf{r}_{s/i} \iff \left(\ddot{\mathbf{r}}_{s/i}\right)_{grav} = \nabla U, \quad \text{where } U = \mu\frac{1}{||\mathbf{r}_{s/i}||_2} \quad (3.6)$$

Here $\mu = GM$ is the Earth's gravitational parameter, and ∇U is an equivalent representation given by the gradient of the gravity potential. Other literature define U with the opposite sign, but here $U > 0$ is chosen to stay consistent with the convention used by Montenbruck & Gill. Their literature explains that this model is inaccurate due to the Earth's mass being unhomogeneously distributed through its volume, and because its rotational velocity causes its shape to bulge around the equator [21]. They go on to present an extension of Equation 3.6 to account for these irregularities in the Earth's gravitational field, starting with a generalization of the gravity potential by summing up the contributions from all internal mass elements. With $\rho(\mathbf{r}_{p/i}^f)$ representing the density at some point p, and $\{\mathbf{r}_{s/i}^f, \mathbf{r}_{p/i}^f\}$ denoting the positions of the satellite and the point in ECEF respectively, the general gravity potential can be expressed as:

$$U = G\int \frac{1}{||\mathbf{r}_{s/i}^f - \mathbf{r}_{p/i}^f||_2}dm = G\int \frac{1}{||\mathbf{r}_{s/i}^f - \mathbf{r}_{p/i}^f||_2}\rho(\mathbf{r}_{p/i}^f)d^3\mathbf{r}_{p/i}^f \quad (3.7)$$

However, the density distribution is not accurately known, which makes the expression impractical. To evaluate the integral further, the fraction can be expanded using a series of Legendre polynomials. The general Legendre polynomial P_{nm} of degree n and order m is defined as:

$$P_{nm}(u) = (1 - u^2)^{m/2} \frac{d^m}{du^m} P_n(u) \tag{3.8}$$

Introducing the spacecraft's geocentric distance $r = ||r_{s/i}||_2$, the latitude ϕ^f and the longitude λ^f allows the satellite's position in the ECEF frame to be expressed in spherical coordinates $\{r, \phi^f, \lambda^f\}$. The superscript f is in this case used to indicate that the angles are Earth-fixed. Using these coordinates together with the associated Legendre polynomials, the gravity potential can be written in its general spherical harmonic form:

$$U = \frac{\mu}{R} \sum_{n=0}^{\infty} \sum_{m=0}^{n} (C_{nm}V_{nm} + S_{nm}W_{nm}), \quad \begin{cases} V_{nm} &= \left(\frac{R}{r}\right)^{n+1} P_{nm}(\sin \phi^f) \cdot \cos m\lambda^f \\ W_{nm} &= \left(\frac{R}{r}\right)^{n+1} P_{nm}(\sin \phi^f) \cdot \sin m\lambda^f \end{cases} \tag{3.9}$$

Here, R denote the Earth's reference radius, and the geopotential coefficients C_{nm} and S_{nm} encode the internal mass distribution's effect on the satellite. Because the longitudinal mass variations are comparatively small, a common simplification is to set $m = 0$, giving the so-called zonal coefficient. Under this assumption, $J_n = -C_n0$ and $W_{n0} = 0$, which significantly simplifies the Equation 3.9. Using the zonal terms up to forth degree, the truncated gravitational potential can be computed from the Legendre polynomials and J-terms in table 3.2.1:

$$
\begin{aligned}
U(r, \phi^f, \lambda^f) &= \frac{\mu}{R} \sum_{n=0}^{4} (C_{n0}V_{n0} + S_{n0}W_{n0}) \\
U(r, \phi^f) &= \frac{\mu}{R} \sum_{n=0}^{4} (C_{n0}V_{n0}) \\
&= \frac{\mu}{R} \left[C_{00}V_{00} + C_{10}V_{10} + C_{20}V_{20} + C_{30}V_{30} + C_{40}V_{40} \right] \\
&= \frac{\mu}{R} \left[\left(\frac{R}{r}\right) - J_2 \left(\frac{R}{r}\right)^3 P_2(\sin \phi^f) \right. \\
&\qquad \left. - J_3 \left(\frac{R}{r}\right)^4 P_3(\sin \phi^f) - J_4 \left(\frac{R}{r}\right)^5 P_4(\sin \phi^f) \right] \\
U(r, \phi^f) &= \frac{\mu}{r} \left[1 - J_2 \left(\frac{R}{r}\right)^2 P_2(\sin \phi^f) \right. \\
&\qquad \left. - J_3 \left(\frac{R}{r}\right)^3 P_3(\sin \phi^f) - J_4 \left(\frac{R}{r}\right)^4 P_4(\sin \phi^f) \right] \\
U(r, \phi^f) &= \frac{\mu}{r} \left[1 - \sum_{n=2}^{4} J_n \left(\frac{R}{r}\right)^n P_n(\sin \phi^f) \right]
\end{aligned}
\tag{3.10}
$$

Among the zonal coefficients, J_2 is by far the most significant, and dominates the non-spherical effects. It captures the Earth's oblateness and produces the well known secular perturbations in the orbital elements, which drifts the right ascension of the ascending node and rotation of the argument of perigee. The higher-degree J_3 and J_4 terms are several orders of magnitude less significant, but still produce a notable perturbation. J_3

induces long-period variations in eccentricity due to asymmetry between the northern and southern hemispheres, while J_4 refines the flatness modelling, and contributes to small corrections to the secular rates caused by J_2 [13, 21, 22]. Inserting this truncated spherical

n	J_n	$P_n(u)$
0	-1	1
1	0	u
2	1.08263×10^{-3}	$\frac{1}{2}(3u^2 - 1)$
3	-2.53266×10^{-6}	$\frac{1}{2}(5u^3 - 3u)$
4	-1.61962×10^{-6}	$\frac{1}{8}(35u^4 - 30u^2 + 3)$

Table 3.2.1: Zonal coefficients and associated Legendre polynomials up to fourth degree. Values courtesy of [23].

harmonic expression into Equation 3.7 yields the acceleration experienced by an arbitrary spacecraft, expressed in the ECEF frame. By computing the gradient, then applying the time-varying transformation in Equation 3.4, the acceleration can then be transformed into the ECI frame:

$$\mathbf{a}^f_{grav} = \left(\ddot{\mathbf{r}}^f_{s/i}\right)_{grav} = \nabla U(r, \phi^f) \iff \mathbf{a}^i_{grav} = \left(\ddot{\mathbf{r}}^i_{s/i}\right)_{grav} = \mathbf{R}^i_f \nabla U(r, \phi^f) \tag{3.11}$$

3.2.2   Atmospheric Drag

Atmospheric drag is the most influential non-gravitational perturbation acting on satellites in LEO. The perturbation is caused by a momentum exchange between the spacecraft's surface and the residual air-molecules encountered along its trajectory. The resulting acceleration will always act opposite to the satellite's velocity, causing a slow deceleration over time. The momentum exchange is typically modelled in the free-molecular flow regime, which assumes that the molecules bouncing off the spacecraft's surface do not interfere with incoming ones. The acceleration can then be expressed using the classical aerodynamic formulation [21, 13]:

$$\mathbf{a}^i_{\text{drag}} = \left(\ddot{\mathbf{r}}^i_{s/i}\right)_{drag} = -\tfrac{1}{2} C_D \frac{A_D}{m} \rho\, v^2_{\text{rel}}\, \hat{\mathbf{v}}^i_{rel} \tag{3.12}$$

In this expression, A_D is the cross-section of the spacecraft perpendicular to the incoming molecular flow, which is often approximated as constant even though it varies with the spacecraft's attitude and geometry [22]. Furthermore, the acceleration magnitude is inversely proportional to the spacecraft's mass m, given by the area-to-mass ratio. The term $\mathbf{v}^i_{rel}$ represents the relative velocity between the satellite and the surrounding atmosphere expressed in ECI. v_{rel} and $\hat{\mathbf{v}}^i_{rel}$ is the velocity's magnitude and unit vector, respectively. Montenbruck & Gill presents a satisfactory first-order approximation where the atmosphere co-rotates with the Earth [21]:

$$\mathbf{v}^i_{rel} = \mathbf{v}^i_{s/i} - \boldsymbol{\omega}^i_{f/i} \times \mathbf{r}^i_{s/i}, \tag{3.13}$$

where $\{\mathbf{r}^i_{s/i}, \mathbf{v}^i_{s/i}\}$ is the position and velocity of an arbitrary satellite s in ECI, and $\boldsymbol{\omega}^i_{f/i}$ is the Earth's angular velocity. The parameter ρ denotes the local atmospheric density, and its modelling is a major source of drag uncertainty because the upper atmosphere is

subject to constant change from solar and geomagnetic activity. A "rough estimate" of the density's dependence on the altitude h is the exponential density model [21, 13]:

$$\rho(h) = \rho_0 \exp\left(-\frac{h - h_0}{H_0}\right), \qquad H_0 = \frac{\mathcal{R}T}{\mu_m g} \qquad (3.14)$$

Here h_0 is the geocentric distance to the Earth's surface, h is the conventional altitude and ρ_0 is the reference density at altitude $h = 0$. H_0 is the density scale height, and is defined as the height where the density is reduced to ρ_0/e. This height is given as a function of Boltzmamnn's constant $\mathcal{R}$, the atmospheric temperature T, the mean molecular mass μ_m and the acceleration magnitude due to gravity g [21, 24].

The final parameter in Equation 3.12 is the drag coefficient C_D. It describes the interaction between the impacting atmospheric molecule and the spacecraft's surface. Its value is dependent on the surface material, gas-surface interaction, temperature and flow regime through complex mechanisms, which makes its calculation non-trivial. However, Montenbruck & Gill reports that typical values of C_D range between $1.5 - 3.0$, and that the initial estimation is commonly corrected through orbit determination [21].

3.2.3 Solar Radiation Pressure

SRP becomes the dominant non-gravitational orbital perturbation acting on a spacecraft for altitudes greater than approximately $800km$. Its influence manifests as long-period variations of the orbital eccentricity, argument of perigee and inclination, especially for satellites with a large area-to-mass ratio. SRP exerts a small force through the absorption or reflection of photons. Both mechanisms transfer momentum from the photons to the surface, generating force proportional to the solar flux and directed away from the Sun. As described by Montenbruck & Gill, the resulting acceleration depends on the geometry between the Sun direction vector $\mathbf{r}^i_{Sun/s}$ and the unit vector normal to the spacecraft's flat surface $\hat{\mathbf{n}}_s$ [21]:

$$\mathbf{a}^i_{SRP} = \left(\ddot{\mathbf{r}}^i_{s/i}\right)_{SRP} = -P_{Sun} \frac{\mathrm{AU}^2}{||\mathbf{r}^i_{Sun/s}||^2_2} \frac{A_R}{m_s} \cos(\theta) \left[(1 - \varepsilon)\hat{\mathbf{r}}^i_{Sun/s} + 2\varepsilon \cos(\theta)\hat{\mathbf{n}}_s\right] \qquad (3.15)$$

P_{Sun} is the radiation pressure given by the solar flux at one Astronomical Unit (AU), which is defined as mean radius of Earth's orbit. Numerical values for this radiation pressure and one AU in meters are show table .0.1. $\{\mathbf{r}^i_{Sun/s}, \hat{\mathbf{r}}^i_{Sun/s}\}$ is the Sun's position relative to the satellite and its corresponding unit vector, respectively. A_R/m_s is the ratio between the cross-section area perpendicular to $\hat{\mathbf{r}}^i_{Sun/s}$ and the satellite's mass. θ represents the angle between the incoming radiation $\hat{\mathbf{r}}^i_{Sun/s}$ and n_s, and ε represents the surface reflectivity. However, Montenbrock & Gill argues that the assumption $\theta = 0$ is sufficient for many applications. Using this assumption, Equation 3.15 can be simplified to the so-called "cannonball" model by introducing a radiation pressure coefficient $C_R = 1 - \varepsilon$ [21]:

$$\mathbf{a}^i_{SRP} = \left(\ddot{\mathbf{r}}^i_{s/i}\right)_{SRP} = -P_{Sun} C_R \frac{A_R}{m_s} \frac{\mathbf{r}^i_{Sun/s}}{||\mathbf{r}^i_{Sun/s}||^3_2} \mathrm{AU}^2 \qquad (3.16)$$

3.2.4   Third-Body Perturbations

In addition to the Earth's gravity field, a satellite in orbit around Earth also experiences gravitational pull from the Sun and Moon, causing a perturbing acceleration. Although these bodies are distant, their great masses still produce accelerations comparable to higher-order geopotential terms, especially for satellites in Medium Earth Orbit (MEO) or higher. As described by Montenbruck & Gill, the perturbing acceleration from a massive third-body B is obtained by subtracting its acceleration on the Earth from its acceleration on the spacecraft through Newton's gravitational law [21]. Its formulation in the ECI frame is:

$$\mathbf{a}_B^i = \left(\ddot{\mathbf{r}}_{s/i}^i\right)_B = \mu_B \left(\frac{\mathbf{r}_{B/i}^i - \mathbf{r}_{s/i}^i}{||\mathbf{r}_{B/i}^i - \mathbf{r}_{s/i}^i||_2^3} - \frac{\mathbf{r}_{B/i}^i}{||\mathbf{r}_{B/i}^i||_2^3} \right) = \mu_B \left(\frac{\mathbf{r}_{B/s}^i}{||\mathbf{r}_{B/s}^i||_2^3} - \frac{\mathbf{r}_{B/i}^i}{||\mathbf{r}_{B/i}^i||_2^3} \right) \quad (3.17)$$

Here $\mu_B = GM_B$ is the massive body's gravitational parameter, $\mathbf{r}_{B/s}^i$ is the body's position relative to the satellite, and $\{\mathbf{r}_{B/i}^i, \mathbf{r}_{s/i}^i\}$ denote the geocentric coordinates of the body and satellite, respectively. This differential formulation in Equation 3.17 ensures that only the perturbing acceleration is expressed. Furthermore, Montenbruck & Gill explains how the perturbing gravitational attraction on a satellite changes direction relative to the Earth during its orbit. The tidal forces cause the satellite to experience a pull away from Earth whenever it is on the imaginary line striking through the Earth and the massive body, and a pull towards Earth whenever it is perpendicular to this line [21]. This effect is visualized by the "Earh-Centered Frame" in figure 3.2.2.
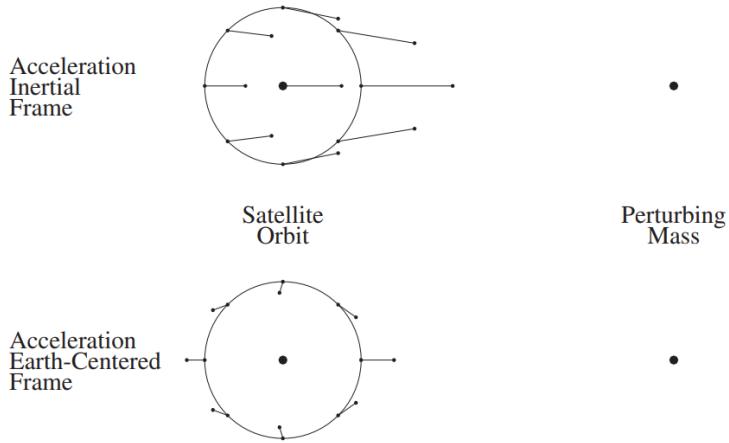
Figure 3.2.2: Tidal forces due to the gravitaional attraction of a distant point-like mass. Courtesy of [21]

The total perturbing acceleration $\mathbf{a}_{B,\text{tot}}^i$ on a satellite from multiple massive bodies, like the Sun and Moon, can be found by summing multiple instances of Equation 3.17 with their corresponding distances and gravitational parameters:

$$\mathbf{a}_{B,\text{tot}}^i = \mathbf{a}_{\text{Sun}}^i + \mathbf{a}_{\text{Moon}}^i \quad (3.18)$$

3.3   Numerical Orbit Propagation

3.3.1   General Formulation

3.3.2   Runge-Kutta Methods

3.3.3   Fixed-Step vs Variable-Step Integration

3.3.4   Numerical Error Sources

3.4   Analytical Orbit Propagation - SGP4

* Claim: Skyfield calls Vallado's SGP4 algorithm

* Include the fact that SGP4 predictions are most accurate around the epoch when the orbital elements are "best".

Two-Line Element (TLE)

FOUR

METHODS

This chapter describes the method used to investigate the differences between the semi-analytical Skyfield SGP4 orbital propagator and a high-fidelity numerical propagator for satellites in LEO. The comparison is performed through a series of simulation-based experiments designed to assess long-term propagation accuracy, sensitivity to perturbation modelling and numerical integration effects. The main goal of this chapter is therefore to present a transparent overview of the simulation environment and the comparison methodology.

A simulation-based approach is adopted for two main reasons. First, the project aims to understand the Skyfield and Basilisk divergence by quantifying individual perturbation effect's impact on predictions and assessing numerical effects. This research question is inherently rooted in simulations, and the comparison in a simulation environment enables systematic variation of conditions to investigate this. Second, in the event that the SGP4 propagation tool is deemed too inaccurate for downstream orbital or formation flight analyses, an alternative propagation tool has to be implemented in its stead. It therefore makes sense to design [WRITE MORE AFTER COMPLETING THE REST OF THE METHODOLOGY CHAPTER]

1. it is useful to compare the SGP4 against a tunable simulation tool in order to get a better understanding of why SGP4 predictions drift over time. This would be harder to deduce from experimental data alone 2. In the event that the SGP4 propagation tool is deemed too inaccurate for downstream orbital or formation flight analyses, an alternative simulator has to be implemented in its stead. It therefore makes sense to design an

4.1   Literature Search

The literature review was conducted to build a solid theoretical foundation for the project, and to map out other similar studies. More specifically, the primary objectives were to identify established propagation methods, understand the major orbital perturbations with their relative impact on spacecrafts in LEO, and to review existing studies on prediction error growth of SGP4 and numerical orbital propagators over longer time horizons. Based on these objectives, the literature search and following review was structured around three main themes:

- Orbital propagation methods

- Orbital perturbation modelling

- Prediction error growth

The following subsections will present the structured approach used to collect sources and filter out irrelevant or questionable publications for the literature review. This process will hereby be referred to as *literature search*, and must not be confused with the literature review in chapter 2 that analyses and discusses the sources provided by the search.

4.1.1   Sources & Search Strategy

The literature search was initially focused on peer-reviewed journal articles accessed through Scopus and relevant papers provided through academic supervision. As the project matured and new relevant subjects became apparent, the search was later expanded to include books, master's theses and additional journal publications through Google Scholar. For astrodynamical models and perturbation effects, two highly credited textbooks were used extensively, particularly *Satellite orbits: Models, Methods and applications* by Montenbruck and Gill, and *Fundamentals of astrodynamics and applications* by Vallado. These were treated as primary sources and provided the theoretical foundation for the literature review.

The literature search was conducted by defining a structured set of keywords and search phrases within each of the main themes from Section 4.1. As familiarity with the field grew, keywords and search phrases were refined and combined into boolean search strings to focus the search towards specific topics. A comprehensive table of all the keywords, search phrases and time ranges used in the literature search is shown in Table 4.1.1. In this context, *time range* refers to an interval that restricts the search to sources published within the interval. This method is applied in order to ensure that the literature is both relevant and up to date. For both *Orbital propagation methods* and *Orbital perturbation modelling* fields, the time range is set to all sources published after 1960. The large time span was chosen by necessity to include older foundational work because many core astrodynamical models and formulations come from early spaceflight-era literature, as explained in Chapter 2. The time range also served to exclude some of the earliest astrodynamic publications when the field had not yet reached maturity. The *Prediction*

error growth field has a narrower time range, specifically after 2010. This has been chosen to exclude older publications that use outdated numerical models and to focus on the newest accuracy evaluation of the SGP4 propagator.

Field	Keywords	Search Phrases	Time range
Orbital propagation methods	SGP4 Propagation Astrodynamics Orbit Runge-Kutta Satellite LEO	Orbit propagation method Orbital dynamics Astrodynamics Orbital mechanics Numerical orbit integration Analytical orbit propagation Semi-analytical orbit propagation Cowell's method Runge-Kutta orbit propagator High-fidelity orbit simulation Propagator validation	1960–now
Orbital perturbation modelling	Perturbation Disturbance Gravity Model LEO SRP Drag	Orbital perturbation LEO perturbation Gravity field modelling Spherical harmonics Atmospheric drag model LEO drag Exponential atmosphere Solar radiation pressure Cannonball model 3rd body Formation flying perturbation Perturbation comparison	1960–now
Prediction error growth	Simulation Accuracy Error Prediction SGP4 Fixed-step Variable-step Integration	Orbit prediction horizon SGP4 accuracy Propagation uncertainty Long-term orbit accuracy Long-term prediction error Numerical integration error Variable-step integrator error Fixed-step integration error Relative orbital motion accuracy	2010–now

Table 4.1.1: Keywords, search phrases and limited time range used in the literature search for each main theme.

4.1.2   Initial Relevance Screening

Immediate search results were subject to an initial screening to assess their relevance to the project. In this screening process, titles, abstracts and conclusions were reviewed in order to exclude any sources not directly relevant for LEO orbit propagation, perturbation modelling or long time horizon prediction error. The initial search returned approximately 150 sources, which was reduced to 22 remaining sources after the initial relevance screening. The large reduction reflects the broad keyword searches, and the relatively narrow focus of this project.

4.1.3   Quality and Credibility Screening

Following the initial relevance screening, a second screening phase was conducted to assess the quality and credibility of the remaining sources. Each source's credibility was assessed through a total of four criteria. First, the author's expertise and standing in the field is evaluated by checking their previous work. This also helps to distinguish foundational contributors from aiding authors. Second, the reputation of the publishing journal or institution is considered. However, even renowned authors and publishers can still publish flawed work. That is why the two next criteria aim to evaluate their content in more detail. The third criteria detect errors and inconsistencies by cross-checking facts and mathematical formulations. Here, the primary sources from Montenbruck and Vallado [21, 13] was especially important to evaluate astrodynamical models, but other previously assessed independent sources were also used for the same purpose. Finally, the source's methodology and overall structure were evaluated to ensure that final results were produced by using a well thought out approach. After the final screening, the number of remaining sources had been reduced to 13

4.2   Simulation

In order to compare the Skyfield SGP4 predictions against a high-fidelity Basilisk counterpart, a modular simulation framework has been developed in Python. The following subsections will present the high-level structure of this simulator, a deeper understanding of each orbit propagation sub-simulation and its implementation, the data processing methodology, and finally, how the simulator is configured to run specific simulation cases. For future reference, the term *simulator* describes the simulation framework in its entirety, and *sub-simulation* will be used to denote an individual orbital propagator within it.

## 4.2.1   Overall Simulation & Analysis Pipeline
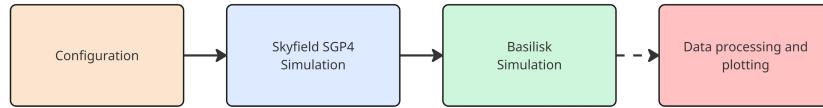
Figure 4.2.1: High-level simulator flow diagram

The overall structure of the simulation framework is illustrated in Figure 4.2.1, which presents a high-level abstraction of the simulator as a sequence of modules. The simulator is composed of four modules: a configuration module, a semi-analytical orbit propagation module based on Skyfield SGP4, a numerical orbit propagation module based on Basilisk, and a data processing and plotting module. A more detailed view of the internal processes executed within each module, from configuration up to and including the Basilisk simulation module, is shown in Figure 4.2.2. This diagram is divided into five separate layers meant to represent different aspects of the simulator structure. The top and bottom layers represent the simulator inputs and outputs, respectively. The middle layer show the modules divided into program blocks, and its adjacent layers show how object instances are passed between them. Finally, the *Data processing and plotting* module is omitted from this diagram to avoid unnecessary complexity, and because it is explained in greater detail in Section 4.2.3.
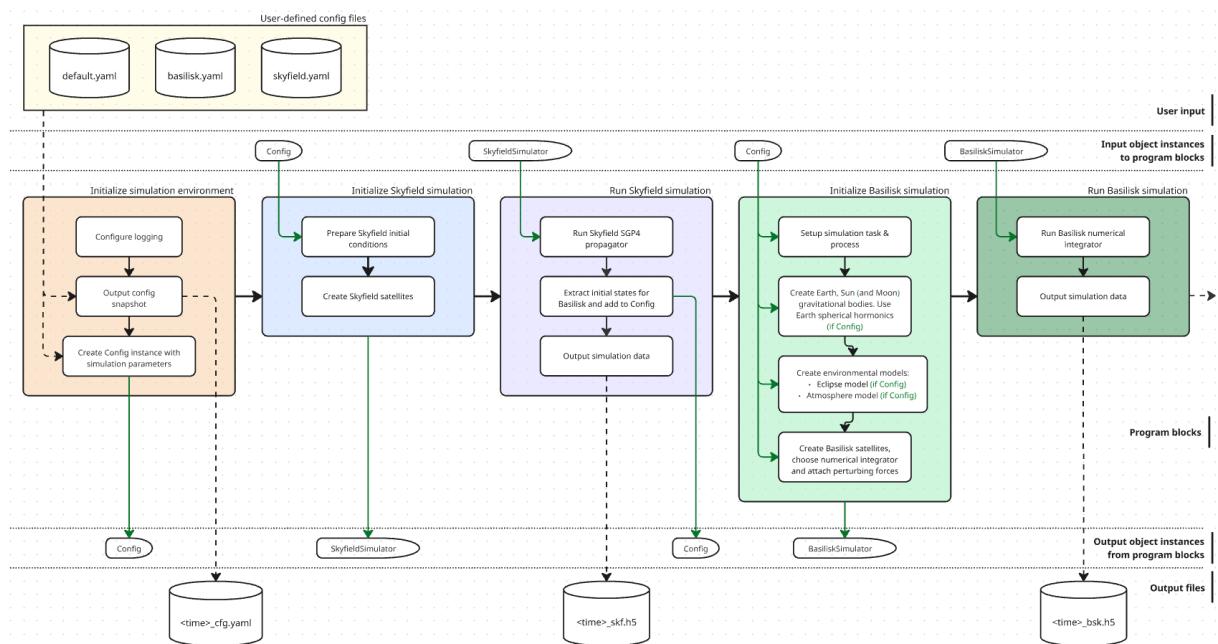
Figure 4.2.2: Detailed simulator flow diagram

The configuration module is responsible for initializing the global simulation environment. Three user-defined configuration files specify the simulation start time and duration, satellite properties and TLEs, numerical integrator settings and perturbation models. These configuration files are parsed and combined into a single configuration instance that is shared by both Skyfield and Basilisk sub-simulations to ensure consistency between the

propagators. As part of this process, a snapshot of the combined configuration is out-putted as `<time>_cfg.yaml`, where `<time>` denotes real-world timestamp for when the simulator was executed. This snapshot is important for traceability because it enables checking what simulation configuration was used to produce a set of simulator outputs at a later stage.

Following configuration, the Skyfield SGP4 sub-simulation is initialized and executed. Using the specified TLEs and simulation parameters, Skyfield propagates the satellite states over the full simulation duration. In this process, satellite translational states are evaluated at discrete time intervals defined by the simulation configuration, and the internal workings of the SGP4 algorithm. After completion, the resulting ECI position and velocities are outputted as a data file named `<time>_skf.h5`, where `<time>` is the same timestamp used by the configuration module. The Skyfield SGP4-propagated satellite states at the initial simulation time are extracted and used to define the initial conditions for the Basilisk sub-simulation. This step is necessary because Basilisk does not natively support TLE-based initialization, and this approach ensures that both propagation methods start from identical initial states.

Next, the Basilisk sub-simulation is initialized. Compared to Skyfield, this initialization involves additional steps, including the creation of simulation processes, tasks, spacecraft and recorders required by the Basilisk framework, as well as defining numerical integrators and environmental models. The inclusion of individual perturbation models such as Earth's spherical harmonics, atmospheric drag, solar radiation pressure, and third-body gravitational effects, is controlled by the global configuration. In the detailed flow diagram in Figure 4.2.2, these conditional steps are indicated by the annotation "if Config", showing that these models will only be created if specified by the simulator configuration. Once initialized, the Basilisk simulation is run, and the resulting satellite ECI state trajectories are outputted as a file named `<time>_bsk.h5`.

The final module in the pipeline is the data processing and plotting module. In Figure 4.2.1, the flow from the Basilisk simulation to this module is denoted by a dashed arrow. This notation indicates that the module can either be executed directly as part of the simulation run, or be called independently at a later time. When executed in series with the other modules, it loads the newly generated Skyfield and Basilisk output files and performs the data processing required to generate the plots specified in the global configuration. Depending on the requested output, this may involve simple visualization of position and velocity data, or additional data processing steps such as reference frame transformations for relative motion analysis. The data processing specifics are presented in greater detail in Section 4.2.3. Alternatively, the same module can be configured to operate on previously generated simulation data, allowing analyses to be repeated or extended without running the computationally expensive propagations.

4.2.2 Simulator Inputs

Simulation cases and propagation settings are defined through a set of three user-defined configuration files, as shown by the yellow box in the *User input* layer of Figure 4.2.2. The global simulation configuration is specified in the file `default.yaml`, which defines all

parameters required to describe the simulation scenario. This file contains the simulation start time and duration, satellite parameters and TLEs for both the leader and follower satellite, as well as settings related to data processing and plotting. With this structure, the global configuration ensures consistency across all sub-simulation. A comprehensive list of all simulator input parameters is displayed in Table 4.2.1.

Config file	Input parameters	Unit
default.yaml	Simulation start time	UTC
	Simulation duration	h
	For each satellite:	-
	TLE	-
	Mass	kg
	Drag coefficient	-
	Cross-section area perpendicular to velocity	m^2
	Radiation pressure coefficient	-
	Cross-section area perpendicular to the Sun-vector	m^2
	Data processing and plotting flags	-
skyfield.yaml	SGP4 time step size	sec
basilisk.yaml	Fixed-step size	sec
	Numeric integrator	-
	Spherical harmonics degree	-
	Enable spherical harmonics flag	-
	Enable drag flag	-
	Enable solar radiation pressure flag	-
	Enable Sun third-body pull flag	-
	Enable Moon third-body pull flag	-

Table 4.2.1: A comprehensive list of all simulator input parameters across all config files.

The parameters that apply to a specific propagator are placed in its corresponding configuration file. For instance, the Skyfield configuration file, `skyfield.yaml`, contains a single parameter specifying the time interval between SGP4 state evaluations. The Basilisk configuration file, `basilisk.yaml`, contains parameters related to numerical propagation, including the choice of numerical integrator, fixed integration time step (when applicable), the degree of the Earth's spherical harmonics model, and boolean flags for enabling/disabling any of the perturbation effects

4.2.3 Data Processing & Comparison Metrics

4.2.4 Verification & Consistency Checks

4.3 Simulation Setup & Assumptions

The simulation framework was designed to support multiple simulation experiments with different objectives while maintaining a consistent underlying scenario. Throughout this project, three distinct simulation experiments were conducted, each addressing a specific research goal. All experiments were based on the same orbital case, defined by a common start time, identical satellite parameters, and the same leader-follower formation geometry. Differences between the experiments were introduced only through changes in simulation duration and Basilisk-specific configuration settings. This approach ensures that observed differences in the results can be attributed to propagation method, perturbation modelling, or numerical integration choices rather than changes in the underlying scenario. The following subsections will first present how the final simulation configuration parameters were determined, then explain how they were methodically varied between experiments to isolate different effects.

4.3.1 Satellite Modelling

Both the leader and follower satellites are modelled to represent a generic 6U CubeSat covered by solar panels. The physical parameters used in the experiments are selected to be representative of this shape, and are assumed to be constant throughout the simulation duration. Identical parameters are used for both satellites in order to isolate differences arising from orbit propagation rather than spacecraft properties. The typical mass of such a spacecraft is reported to be approximately $m_s = 6.0$kg. Attitude dynamics are not modelled, and the satellites are assumed to maintain a worst-case fixed orientation to induce the largest perturbation forces from drag and SRP simultaneously. This means that the largest satellite face is pointing towards velocity vector and Sun direction at all times, even though this attitude is not always physically feasible. The corresponding cross-section areas normal to these directions are therefore $A_D = A_{SRP} = 0.3m \times 0.2m = 0.06m^2$.

The satellites' drag coefficients are chosen to approximate the atmosphere-satellite interactions for non-spherical spacecraft in LEO. Quinci writes in his paper that a reasonable drag coefficient is 2.2 for a typical spacecraft [25], which is backed up by Montenbruck and Gill who propose a crude estimate in the range $2.0 - 2.3$ [21]. Therefore, the drag coefficient is set to $C_D = 2.2$. Continuing with the assumption that both satellites are covered by solar panels, Montenbruck and Gill documents that a typical value for solar radiation pressure coefficient is $C_R = 1.21$ because of the panels' reflectivity, and is therefore adopted for this study.

4.3.2 Orbital Configuration

The leader satellite orbit is defined using a real TLE corresponding to the HYPSO-1 satellite. HYPSO-1 is a 6U CubeSat operating in LEO, making it a suitable reference for this study both in terms of orbital regime and spacecraft scale. Using a real TLE ensures that the baseline orbit includes realistic orbital elements and atmospheric drag characteristics, as reflected by the TLE's ballistic coefficient parameter. The TLE used to initialize the leader satellite orbit is shown below for reproducibility:

```
HYPSO-1
1 51053U 22002BX   25296.93021535  .00034531  00000+0  64114-3 0  9996
2 51053  97.3166    6.7052 0004161  83.3535 276.8189 15.48851464210108
HYPSO-1-follower
1 51053U 22002BX   25296.93021535  .00034531  00000+0  64114-3 0  9996
2 51053  97.3166    6.7052 0004161  83.3535 266.8189 15.48851464210108
```

The follower satellite orbit is derived by modifying the leader's TLE such that the follower trails the leader by a fixed angular separation of 10° along the same orbital plane. This is achieved by adjusting the phase of the orbit while keeping all other orbital elements identical. The resulting configuration forms a simple leader-follower formation with a constant nominal along-track separation and no relative inclination or eccentricity offsets. Only a single formation geometry is considered in this project, and no active formation control or orbital maneuvers are modelled. This simplified configuration is chosen to enable a clear comparison of relative motion predictions between orbit propagation methods

4.3.3 Simulation Experiments

Three simulation experiments were conducted to address the different research questions of the project. In all experiments, satellite parameters, TLEs, formation geometry, and Skyfield SGP4 step size were kept identical, and the simulation start time was chosen to match the TLE epochs. This ensured that differences between experiments arise solely from controlled changes, and not because of the underlying simulation case or differences in Skyfield SGP4 propagation. An overview of the three experiments is provided in Table 4.3.1, which summarizes their respective purposes, comparison methods, simulation durations, Basilisk numerical integrators, and enabled perturbations. The remaining input parameters were adjusted between experiments according to their specific focus, as detailed in the table.

Experiment #	1	2	3
Purpose	To investigate the Skyfield SGP4 and Basilisk propagation differences	To quantify the individual perturbation effect's impact on the satellite orbits	To study the numerical integrator's impact on propagation accuracy
Comparison method	Single Basilisk output compared directly against Skyfield baseline	Multiple Basilisk outputs compared against Basilisk reduced perturbation baseline	Multiple Basilisk outputs compared against Skyfield baseline
Simulation duration	168 hours	96 hours	96 hours
Skyfield step size	1 seconds	5 seconds	5 seconds
basilisk step size	1 seconds	5 seconds	Subject to change
Basilisk numerical integrator	RK4	RK4	Subject to change
Enabled perturbations	All	Subject to change	All

Table 4.3.1: Overview of how the three experiments differs from each other in purpose, comparison method and configuration.

The first experiment focuses on evaluating the long-term disagreement between the Skyfield SGP4 propagator and the high-fidelity numerical propagation using Basilisk. In this experiment, the maximum simulation duration 168 hours (7 days) is used, and all orbital perturbations are enabled. Both Skyfield and Basilisk are configured to use a 1-second step size, with Basilisk using the fixed-step RK4 numerical integrator. This configuration represents the highest-fidelity numerical propagation used in the project and serves as the primary reference for assessing SGP4 accuracy over extended time horizons.

The second experiment aims to quantify the relative impact of individual orbital perturbations on the propagated satellite trajectories. For this experiment, the simulation duration is reduced to 96 hours, and both the Skyfield SGP4 and Basilisk propagation step sizes are increased to 5 seconds, as summarized in Table 4.3.1. This modification is applied to limit computational cost, since multiple Basilisk simulations are executed with different combinations of enabled perturbation models. Basilisk employs a fixed-step RK4 integrator, while the enabled perturbations are varied between simulation runs. Each resulting Basilisk trajectory is compared against a reduced-perturbation Basilisk baseline, allowing the relative contribution of individual perturbation effects to be isolated.

The third experiment investigates the influence of numerical integration settings on the propagated satellite trajectories. The simulation duration is again set to 96 hours, while the Skyfield SGP4 step size remains fixed at 5 seconds. Multiple Basilisk simulations

are performed using different numerical integrators and, where applicable, different step sizes, as indicated in Table 4.3.1. All Basilisk configurations are compared against a single Skyfield SGP4 baseline trajectory in order to assess the sensitivity of the propagation results to numerical integration choices.

FIVE

RESULTS

5.1 Simulation Parameters

Parameter	Value	Unit
C_D	$1.5 - 3$	-
A_D	-	-
C_R	$-$	-
A_{SRP}	-	-

Table 5.1.1: Physical constants and associated numerical value. J-terms courtesy of [23].

5.2 Prelim results

The current simulator implementation has been used to generate preliminary results for a two-satellite scenario consisting of one chief and one follower spacecraft initialized on different orbital planes in LEO. Skyfield's SGP4 model serves as the baseline, while the Basilisk simulation includes gravity-gradient effects, solar radiation pressure, and lunar third-body pull. Atmospheric drag has not yet been implemented, and both propagators are run over the same integration time for direct comparison.

Figure 1 and 2 show the ECI position and velocity differences between Basilisk and SGP4 for the chief and follower spacecraft, respectively. Figure 3 presents the difference in relative motion between the two spacecrafts expressed in the RTN frame. In all cases, the divergence begins small but increases steadily over time. This divergence can be attributed to a combination of intrinsic numerical simulator difference and additional physical perturbations included only in the Basilisk simulation. The large discrepancy

visible in the relative-motion plot indicates that a formation-keeping delta-V analysis performed with the two simulation frameworks would yield significantly different results after 24 hours. Further testing and analysis are required to determine how much of this divergence is caused by numerical effects versus physical modelling differences.

Below is a list over all types of plots that I deem valuable for the specialization project. Each plot-type shall be justified by a short description of its usefulness.

5.2.1 Simulator output difference plots

Show the absolute value logarithmic difference between the simulators. This will make it easier to see the small differences for times smaller than 6 hours, and the big differences after 24 hours. Do this for both the absolute pos/vel difference plot, and the relative formation pos/vel plots.

5.2.2 R

SIX

DISCUSSION

Discuss your results here.

6.1 Future work

Include a section about what should or could be done in future research, or explain any recommended next steps based on the results you got. This should be the last section in the discussion.

How do zxc here's to all the idk This situation is starting to become pretty dire

6.2 Methodological Limitations

SEVEN

CONCLUSIONS

Give a concise summary of your research and finding here, and include a short summary of any future work as well.

[1] NASA Earthdata. *GNSS - Global Navigation Satellite System*. Accessed: 2025-11-23. 2024. URL: https://www.earthdata.nasa.gov/data/space-geodesy-techniques/gnss.

[2] Harry W. Jones. "The Recent Large Reduction in Space Launch Cost". In: *48th International Conference on Environmental Systems (ICES)*. ICES-2018-81. Albuquerque, New Mexico, July 2018, pp. 1–10. URL: https://ntrs.nasa.gov/citations/20200001093.

[3] *Hva er jamming, spoofing og meaconing?* FFI Factsheet. Accessed: 2025-11-21. Norwegian Defence Research Establishment (FFI), 2024.

[4] Norwegian Defence Research Establishment (FFI). *Jamming - a technological cat-and-mouse game*. https://www.ffi.no/en/news/jamming--a-technological-cat-and-mouse-game. Accessed: 2025-02-20. 2024.

[5] GPSJam Project. *GPSJam - Real-time GNSS Interference Map*. https://gpsjam.org. Accessed: 2025-11-21. 2025.

[6] Shuanggen Jin and Attila Komjathy. "GNSS Reflectometry and Remote Sensing: New Objectives and Results". In: *Advances in Space Research* 46.1 (2010), pp. 111–117. DOI: 10.1016/j.asr.2010.01.014. URL: https://www.sciencedirect.com/science/article/pii/S0273117710000499?casa_token=Oz4kQjAlYwsAAAAA:STxQm3Wyqd2XvnpbveQhRXNvqUOfPIugKy2wwwYIkM65IhS2z184eO7fH4z2QJhcTMW1f3IT.

[7] C. Hall and R. Cordey. "Multistatic Scatterometry". In: *Proceedings of the IEEE International Geoscience and Remote Sensing Symposium (IGARSS)*. IEEE. Edinburgh, Scotland, 1988, pp. 561–562.

[8] NTNU SmallSat Lab. *CubeSat Concept Using GNSS-R*. https://www.ntnu.edu/smallsat/gnss-r. Accessed: 2025-11-21. 2025.

[9] Scott Gleason et al. "Geolocation, Calibration and Surface Resolution of CYGNSS GNSS-R Land Observations". In: *Remote Sensing* 12.8 (2020), p. 1317. DOI: 10.3390/rs12081317. URL: https://www.mdpi.com/2072-4292/12/8/1317.

[10] Saika Aida and Michael Kirschner. "Accuracy Assessment of SGP4 Orbit Information Conversion into Osculating Elements". In: (2013). Retrieved from user-provided document, pp. 1–8. URL: https://elib.dlr.de/87081.

[11] Victor Szebehely. "The History and Background of Astrodynamics". In: *Acta Astronautica* 20 (1989), pp. 79–81.

[12]   Isaac Newton. *Philosophiæ Naturalis Principia Mathematica*. Londini: Jussu Societatis Regiæ ac Typis Josephi Streater, 1687.

[13]   David A. Vallado. *Fundamentals of Astrodynamics and Applications*. Springer, 2001. URL: https://books.google.no/books?id=PJLlWzMBKjkC.

[14]   Zac Yung-Chun Liu et al. "Improved Orbital Propagator Integrated with SGP4 and Machine Learning". In: *AIAA/USU Small Satellite Conference*. 2021. URL: https://digitalcommons.usu.edu/smallsat/2021/all2021/193.

[15]   Dave Conkey and Mitchell Zielinski. "Assessing Performance Characteristics of the SGP4-XP Propagation Algorithm". In: *Advanced Maui Optical and Space Surveillance Technologies Conference (AMOS)*. 2022. URL: https://amostech.com/TechnicalPapers/2022/Poster/Conkey.pdf.

[16]   Giacomo Acciarini, Atilim Günes Baydin, and Dario Izzo. "Closing the Gap Between SGP4 and High-Precision Propagation via Differentiable Programming". In: *Acta Astronautica* (2024). URL: https://www.sciencedirect.com/science/article/pii/S0094576524006374.

[17]   Mariusz Eivind Grøtte et al. "Spacecraft Attitude and Angular Rate Tracking using Reaction Wheels and Magnetorquers". In: *IFAC-PapersOnLine* 53.2 (2020), pp. 14819–14826. DOI: 10.1016/j.ifacol.2020.12.1924. URL: https://www.sciencedirect.com/science/article/pii/S2405896320325441.

[18]   Gabriel Popescu. "Pixel Geolocation Algorithm for Satellite Scanner Data". In: (2014). PDF provided by user; publication year and journal not specified. URL: https://www.researchgate.net/publication/311807426_Pixel_geolocation_algorithm_for_satellite_scanner_data.

[19]   Sascha Metz. "Implementation and Comparison of Data-Based Methods for Collision Avoidance in Satellite Operations". Master's Thesis. Darmstadt, Germany: Technische Universität Darmstadt, 2020. URL: https://www.researchgate.net/publication/344268107_Master_Thesis_Implementation_and_comparison_of_data-based_methods_for_collision_avoidance_in_satellite_operations.

[20]   John Stryjewski. *Coordinate Transformations*. Technical Report. Version 08/19/20. MIT Lincoln Laboratory, Aug. 2020. URL: https://x-lumin.com/wp-content/uploads/2020/09/Coordinate_Transforms.pdf.

[21]   Oliver Montenbruck and Eberhard Gill. *Satellite Orbits: Models, Methods and Applications*. 1st ed. Corrected 4th printing 2012. Berlin, Heidelberg: Springer, 2000. ISBN: 978-3-540-67280-7. URL: https://ftp.space.dtu.dk/pub/nio/Macau/Montenbruck_2000_SatelliteOrbits.pdf.

[22]   Christopher W. T. Roscoe et al. "Force Modeling and State Propagation for Navigation and Maneuver Planning for CubeSat Rendezvous, Proximity Operations, and Docking". In: *Proceedings of the AAS/AIAA Spaceflight Mechanics Meeting*. Applied Defense Solutions. Columbia, Maryland, 2014. URL: https://www.scopus.com/pages/publications/84898934271?origin=resultslist.

[23]   Weichao Zhong and Pini Gurfil. "Mean Orbital Elements Estimation for Autonomous Satellite Guidance and Orbit Control". In: *Journal of Guidance, Control, and Dynamics* 36.6 (2013), pp. 1624–1641. DOI: 10.2514/1.60701. URL: https://www.researchgate.net/publication/260501946_Mean_Orbital_Elements_Estimation_for_Autonomous_Satellite_Guidance_and_Orbit_Control.

[24]   Australian Space Academy. *Terrestrial Atmosphere Modelling.* https://www.spaceacademy.
       net.au/watch/debris/atmosmod.htm.

[25]   Alessio Quinci. *Attitude Control System Design of an Earth-Pointing 6U CubeSat
       in Low Earth Orbit.* Tech. rep. Accessed: 2025-12-10. Polytechnic of Milan, 2021.
       URL: https://d1wqtxts1xzle7.cloudfront.net/86542048/10531692_Quinci-
       libre.pdf.

APPENDICES

A - GITHUB REPOSITORY

All code and latex-files used in this document are included in the Github repository linked below. Further explanations are given in the readme-file.

Specialization project report LaTeX repository link

- https://github.com/chystad/Specialization-Project-Report-LaTeX-

Orbit Simulator repository link

- https://github.com/chystad/Orbit_Simulator

Numerical Values for Physical Constants

$Constant$	$Value$	$Unit$
J_0	-1	-
J_1	0	-
J_2	1.08263×10^{-3}	-
J_3	-2.53266×10^{-6}	-
J_4	-1.61962×10^{-6}	-
P_{Sun}	$4.578299965 \times 10^{-6}$	Ws/m^3
$1AU$	149597871	km
R	6378136.6	m
H_0	7200	m
ρ_0	1.225	kg/m^3
$-$	$-$	$-$
$-$	$-$	$-$
$-$	$-$	$-$

Table .0.1: Physical constants and associated numerical value. J-terms courtesy of [23].